ChemPubSoc Europe

DOI: 10.1002/open.201700110

Open Access ChemistryOPEN Full Papers

The Design of Radical Stacks: Nitronyl-Nitroxide-Substituted Heteropentacenes

Evgeny Tretyakov[+],[a, b] Ashok Keerthi[+],[c] Martin Baumgarten,*[c] Sergey Veber,[b, d] Matvey Fedin,[b, d] Dmitry Gorbunov,[b, e] Inna Shundrina,[a] and Nina Gritsan[b, e]

The first alkyl chain-anchored heteropentacene, dithieno[2,3-*d*;2′,3′-*d*′]benzo-[1,2-*b*;3,4-*b*′]dithiophene (DT*m*BDT), mono- or disubstituted with a nitronyl nitroxide group has been prepared through a cross-coupling synthetic procedure of the corresponding dibromo-derivative (Br_2-DT*m*BDT) with a nitronyl nitroxide-2-ide gold(I) complex. The synthesized nitroxides possess high kinetic stability, which allowed us to investigate their structure and thermal, optical, electrochemical, and magnetic properties. Single-crystal X-ray diffraction of both mono- and diradicals revealed that the nitronyl nitroxide group lies almost in the same plane as the nearest side thiophene ring. Such arrangement favors formation of edge-to-edge dimers, which then form close π-stacks surrounded by interdigitating alkyl chains. Before melting, these nitronyl nitroxide radical substituted molecules undergo at least two different phase transitions (PTs): for the monoradical, PTs are reversible, accompanied by hysteresis, and occur near 13 and 83 °C; the diradical upon heating shows a reversible PT with hysteresis in the temperature range 2–11 °C and an irreversible PT near 135 °C. PTs of this type are absent in Br_2-DT*m*BDT. Therefore, the step-by-step substitution of bromine atoms by nitronyl nitroxide groups changes the structural organization of DT*m*BDT and induces the emergence of PTs. This knowledge may facilitate crystal engineering of π-stacked paramagnets and related molecular spin devices.

1. Introduction

Stable radical moieties covalently linked to acenes have attracted much attention owing to their propensity to assemble into stable stack structures or columnar high-spin structures with promising electronic and magnetic properties.[1–8] The π–π interaction provides the clear packing force for formation of conducting stacks. Through the fusion of five-membered rings, such as thiophenes, acenes gain the capacity for S–S and S–π dipolar interactions that provide a new type of motifs and new electronic properties.[9] This is one of the reasons why thienoacenes, especially those with thieno[3,2-*b*]thiophene units, have become popular in recent years.[10–15] In particular, a new planar heteroacene building block, dithieno[2,3-*d*;2′,3′-*d*′]benzo-[1,2-*b*;3,4-*b*′]dithiophene (DT*m*BDT)[16] was designed to address solubility issues by introducing alkyl chains at the bay positions and to enhance the possibilities for chemical functionalization at the terminal positions (without disturbing the planarity of the core) for various applications in organic electronics.[17–19] Therefore, it is intriguing to prepare spin-bearing DT*m*BDT molecules and to study their structures and inherent properties.

Herein, we report the synthesis and characterization of neutral paramagnetic DT*m*BDT derivatives carrying one or two nitronyl nitroxide moieties, namely, monoradical NNBr-DT*m*BDT and diradical NN_2-DT*m*BDT. It was found that the step-by-step substitution of bromine atoms by nitronyl nitroxide groups preserves the ability of DT*m*BDT to form close stacks, but organized in a different manner. Moreover, for the mono- and diradical, both the reversible and irreversible phase transitions (PTs) have been studied in detail by using differential scanning calorimetry, variable-temperature Fourier transform infrared (FTIR), and electron paramagnetic resonance (EPR) spectroscopy, as well as quantum-chemical calculations.

[a] *Prof. E. Tretyakov,[+] Dr. I. Shundrina*
N. N. Vorozhtsov Institute of Organic Chemistry
9 Ac. Lavrentiev Avenue, Novosibirsk 630090 (Russia)

[b] *Prof. E. Tretyakov,[+] Dr. S. Veber, Prof. M. Fedin, D. Gorbunov, Prof. N. Gritsan*
Novosibirsk State University
2 Pirogova Str., Novosibirsk 630090 (Russia)

[c] *Dr. A. Keerthi,[+] Prof. M. Baumgarten*
Max Planck Institute for Polymer Research
Ackermannweg 10, Mainz 55128 (Germany)
E-mail: martin.baumgarten@mpip-mainz.mpg.de

[d] *Dr. S. Veber, Prof. M. Fedin*
International Tomography Center
3a Institutskaya Str., Novosibirsk 630090 (Russia)

[e] *D. Gorbunov, Prof. N. Gritsan*
V. V. Voevodsky Institute of Chemical Kinetics and Combustion
3 Institutskaya Str., Novosibirsk 630090 (Russia)

[+] *These authors contributed equally to this work*

Supporting Information and the ORCID identification number(s) for the author(s) of this article can be found under: https://doi.org/10.1002/open.201700110.

2. Results and Discussion

2.1. Synthesis

The synthesis of monoradical NNBr-DT*m*BDT and diradical NN_2-DT*m*BDT was carried out by using a palladium-catalyzed cross-coupling reaction of the dibromo derivative Br_2-DT*m*BDT[16] with triphenylphosphine-gold(I)-(nitronyl nitroxide-2-ide) (Ph_3P-Au-NN)[20] (Scheme 1). Analytically pure samples of the nitroxides were obtained by column chromatography on silica gel, followed by procedures of recrystallization from *n*-hexane and then from a mixture of CH_2Cl_2 and MeOH, which was selected by optimization as the most suitable medium for the growth of crystals. Both nitroxides were comprehensively studied in solution as well as in the solid state.

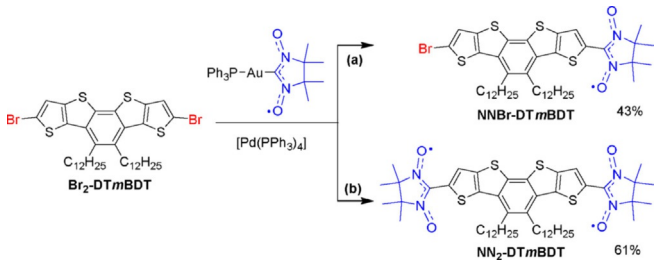

Scheme 1. Synthesis of monoradical NNBr-DT*m*BDT and diradical NN_2-DT*m*BDT: a) 1:1 and b) 1:3 ratios of Br_2-DT*m*BDT and Ph_3P-Au-NN were heated at reflux for 2 or 16 h in THF at 60 °C.

2.2. Properties of Nitroxides in Solution

Figure 1 depicts the electronic absorption spectra of nitroxides NNBr-DT*m*BDT and NN_2-DT*m*BDT in toluene at room temperature. The monoradical NNBr-DT*m*BDT showed a weak structured absorption band in the visible region with maxima at 635, 700, and 779 nm; this pattern is characteristic of nitronyl nitroxide spectra[21] (Figure 1). According to the calculations (Figure S1 a, in the Supporting Information), this band corresponds to a single electronic transition that involves a difference in the electron promotion (a) from the highest occupied molecular orbital (HOMO) to the singly occupied molecular orbital (SOMO) and (b) from the SOMO to the lowest unoccupied molecular orbital (LUMO) presented in Figure S1 b (in the Supporting Information). The intense structured absorption band in the high-energy region with maxima at 395, 374, and a shoulder peaking at 357 nm coincides well with the spectrum of Br_2-DT*m*BDT (Figure S2 in the Supporting Information) and corresponds to π–π^* electronic transitions of the conjugated core of the molecule (DT*m*BDT; the main contribution from the HOMO–LUMO promotion, Figure S1 b (c) in the Supporting Information). The UV/Vis spectrum of the NN_2-DT*m*BDT diradical is very similar to that of NNBr-DT*m*BDT. The only differences are the almost doubled extinction coefficients of the visible-region (low-energy) band owing to the presence of two nitronyl nitroxide moieties and the redshift of the maxima of a high-energy band compared with the monoradical NNBr-DT*m*BDT.

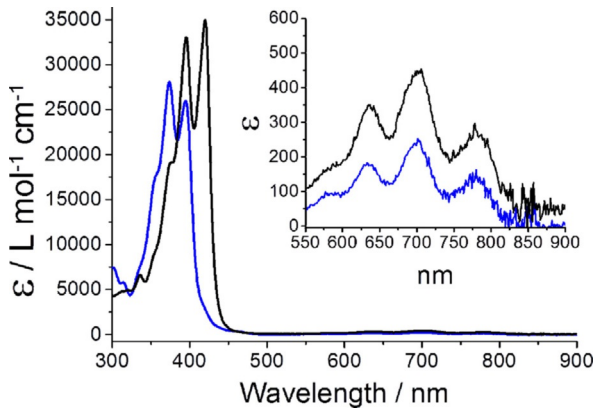

Figure 1. UV/Vis absorption spectra of toluene solutions of monoradical NNBr-DT*m*BDT (blue) and diradical NN_2-DT*m*BDT (black) recorded at room temperature (inset shows the enlarged spectra).

To obtain more detailed information about the electronic structure, electrochemical and electron paramagnetic resonance (EPR) analyses were performed. The electrochemical oxidation (ECO) of monoradical NNBr-DT*m*BDT in CH_2Cl_2 (Figure 2) represents one-electron reversible[22] waves with the half-wave potentials +0.37 V versus Fc/Fc^+ (here and hereinafter) associated with the formation of the corresponding bis(oxoammonium) cation NNBr-DT*m*BDT$^+$. The second ECO peak in the range of +1 V is reasonable to relate to oxidation of the fused heterocyclic moiety because, for example, oxidation potentials for thieno[2,3-*b*]thiophene (1.08 V vs. Fc/Fc^+) and dithieno[3,2-*b*:2′,3′-*d*]thiophene (0.81 V vs. Fc/Fc^+) lie in the same region.[23] The ECO of diradical NN_2-DT*m*BDT revealed the same behavior, namely two-electron waves with half-wave potentials +0.45 V (Figure 2).[24] This means that contrary to the nitronyl nitroxide diradicals with thieno[2,3-*b*]thiophene, thieno[3,2-*b*]thiophene, or dithieno[3,2-*b*:2′,3′-*d*]thiophene linking moieties showing

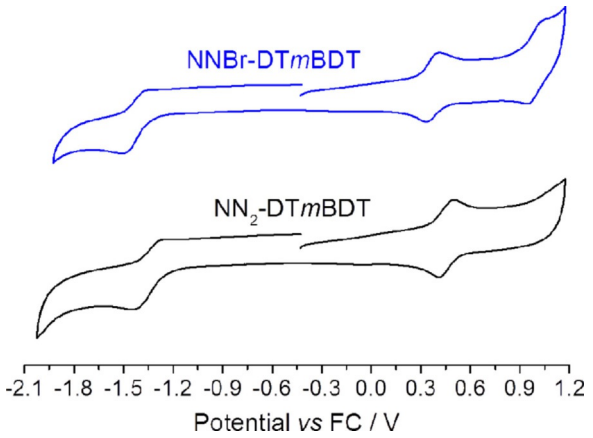

Figure 2. Cyclic voltammetric profiles (0.1 M Bu_4NPF_6 as the supporting electrolyte in dichloromethane with a scan rate of 100 mV s^{-1} and potentials versus the Fc^+/Fc redox couple) of monoradical NNBr-DT*m*BDT (blue) and diradical NN_2-DT*m*BDT (black).

two separated one-electron waves,[9] for NN_2-DT*m*BDT, the oxidation peaks overlap [Eq. (1)]:

$$NN_2\text{-DT}m\text{BDT} \rightleftharpoons \text{NN-DT}m\text{BDT-NN}^{+} \rightleftharpoons NN_2^{2+}\text{-DT}m\text{BDT} \quad (1)$$

Therefore, in the NN_2-DT*m*BDT diradical, two nitronyl nitroxide groups are sequentially oxidized at the same potential, which is shifted toward a more positive voltage compared with that for the NNBr-DT*m*BDT radical.

Electrochemical reduction of both the NNBr-DT*m*BDT radical and the NN_2-DT*m*BDT diradical in CH_2Cl_2, in the potential sweep range of $0 \le E \le 2.0$ V, revealed an irreversible peak at −1.51 and −1.45 V, respectively, which is rather typical for aryl- and heteroaryl-substituted nitronyl nitroxides.[25,26]

The solution EPR spectra of NNBr-DT*m*BDT were recorded at room temperature in toluene at different concentrations. A dilute solution of NNBr-DT*m*BDT ($c \approx 10^{-5}$ M) yielded an EPR spectrum typical of a nitronyl nitroxide radical (Figure 3), which consists of five lines resulting from coupling of the unpaired electron with two equivalent ^{14}N nuclei with a hyperfine coupling (HFC) constant $|A_N| = 0.75$ mT.

The EPR spectra of NN_2-DT*m*BDT in toluene solution are

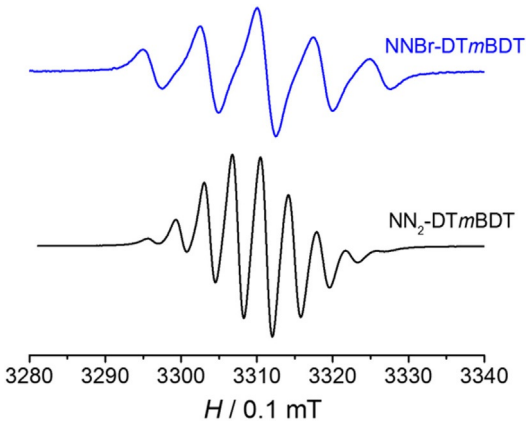

Figure 3. The EPR spectra of monoradical NNBr-DT*m*BDT (blue) and diradical NN_2-DT*m*BDT (black) in a toluene solution at 260 K under isotropic conditions.

characteristic of bis(nitronyl nitroxide) systems with a strong (on the energy scale of EPR spectroscopy) intramolecular exchange interaction (J), which by far exceeds hyperfine coupling ($J \gg A_N$; Figure 3). Indeed, by using the CASSCF and NEVPT2 methods, well-proven in the calculations of J in diradicals,[29b,30] we predict the $|J|$ value to be on the order of a few K (1 K corresponds to 744 mT). The solution spectrum (Figure 3) consists of nine spectral peaks resulting from coupling of two unpaired electrons with four equivalent ^{14}N nuclei; the exchange interaction results in a distance between the lines that equals half of the HFC constant corresponding to the monoradical moiety $|A_N|/2 \approx 0.375$ mT.

Figure 4 shows the EPR spectrum of NN_2-DT*m*BDT in a frozen toluene solution at 150 K. This spectrum is difficult to interpret because the symmetry is partly lost and some anisotropic components may overlap in the $|\Delta m_S| = 1$ region, thus giving rise to a different number of shoulders in the outermost

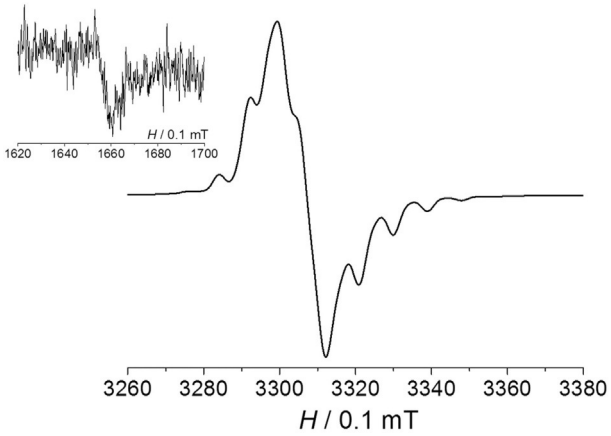

Figure 4. The EPR spectrum of NN_2-DT*m*BDT in frozen toluene at 150 K, with inset of the half field transition.

spectral region (Figure 4). Therefore, the zero-field splitting parameters could be estimated only roughly. Clear evidence for the diradical character, however, stems from the observed $|\Delta m_S| = 2$ transition. The signal has a low signal-to-noise (S/N) ratio because the substantial average value of the N···N, O···O, and N···O distances estimated as 14.8 Å implies small $|D|$ and a weak probability of this transition. Indeed, the distance of 14.8 Å leads to $|D| = 0.9$ mT (8.4×10^{-4} cm^{-1}) based on a point dipole approximation,[27] and this value cannot explain the large enough EPR spectral width. Nonetheless, the density functional theory (DFT) calculations of the spin–spin contribution yielded a similar value: $D = -0.82$ mT (-7.7×10^{-4} cm^{-1}) and $E/D = 0.015$ although typically DFT overestimates spin density delocalization (Figure S15 in the Supporting Information).

2.3. Properties of Nitroxides in the Crystalline State

The structures of radical NNBr-DT*m*BDT and diradical NN_2-DT*m*BDT were successfully confirmed by single-crystal XRD. General crystallographic data and selected geometric parameters for these compounds are summarized in Table 1.

The XRD analysis revealed that nitroxide NNBr-DT*m*BDT crystallizes from a mixture of dichloromethane with methanol in the triclinic $P\bar{1}$ space group. The geometry of the monoradical showed typical bond lengths of the ONCNO moiety in nitronyl nitroxides,[28] with a small torsion angle between the nitronyl nitroxide group and the nearest side thiophene ring ($< 5^{\circ}$). The short intramolecular hydrogen bond O···H–C (2.35 Å) stabilizes the planar structure, and as a result, the short distance between the sulfur atom and nitroxide oxygen (2.84 Å compared with 3.32 Å: the sum of the van der Waals radii of S and O) is observed (Figure 5a).

The crystal packing (Figure S7 in the Supporting Information) of radical NNBr-DT*m*BDT is mainly determined by short intermolecular contacts S···S (3.34 Å) and O···H–C (2.47 Å) leading to formation of centrosymmetrical dimers (Figure 5b), which, in turn, form stacks with short contacts S···S (3.58 Å) and O···H–C_{Me} (2.54 Å). The stacks are separated from each other by interdigitating dodecyl chains (Figure S7 in the Supporting Information). For the magnetically important elements,

Table 1. Crystal data, details of experiments, and selected bond lengths [Å] and angles [°] for radical NNBr-DT*m*BDT and diradical NN_2-DT*m*BDT.

Compound	NNBr-DT*m*BDT	NN_2-DT*m*BDT
formula	$C_{45}H_{64}BrN_2O_2S_4$	$C_{52}H_{76}N_4O_4S_4$
F_W	871.3	949.40
T [K]	130	173
space group, Z	$P\bar{1}$, 2	$P2_1/c$, 8
a [Å]	6.096(2)	25.2251(18)
b [Å]	13.172(5)	16.4013(8)
c [Å]	28.707(11)	27.0452(18)
α [°]	78.500(11)	107.691(5)
β [°]	89.796(10)	
γ [°]	84.085(11)	
V [Å^3]	2247(2)	10660.1(12)
D_c [g cm^{-3}]	1.291	1.183
μ [mm^{-1}]	1.14	1.99
θ_{max} [°]	28	68.1
I_{hkl} (meas/uniq)	27083/10609	89945/19009
R_{int}	0.1269	0.2157
I_{hkl} ($I > 2\sigma I$)	4586	4085
parameters	673	1153
GooF	1.018	0.766
R_1/wR_2	0.0962/0.3119	0.0972/0.3293
$\Delta\rho_{min}$, $\Delta\rho_{max}$ [e Å^{-3}]	−0.93, 1.31	−0.62, 0.51
N–O [Å]	1.277(5), 1.278(8)	1.272(1)–1.313(2)
O_{NO}···S[a] [Å]	2.843(16)	2.753(3)–2.841(4)
O_{NO}···H–C[a] [Å]	2.352(14)	2.359(4)–2.394(0)
∡thiophene–ONCNO[b] [°]	4.9	1.1, 2.6, 5.3, 6.2

[a] Intramolecular distances. [b] Torsion angles [°] between mean planes of the nitronyl nitroxide group and the nearest side thiophene ring.

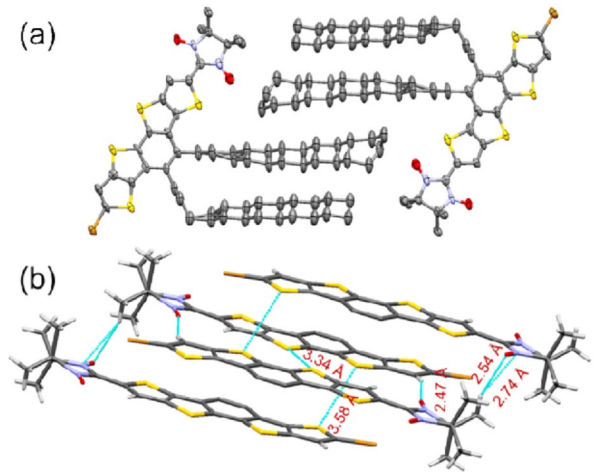

Figure 5. a) A fragment of the crystal packing of radical NNBr-DT*m*BDT with thermal ellipsoids drawn at the 50% probability level (H atoms are omitted for clarity). b) Short contact S···S and O···H–C within dimers and between them (alkyl chains are omitted for clarity).

such an arrangement leads to relatively long intermolecular contacts between nitroxide oxygen atoms (5.15 Å).

In turn, the NN_2-DT*m*BDT diradical crystallizes from a mixture of dichloromethane with methanol in the monoclinic $P2_1/c$ space group with an asymmetric unit containing two diradical molecules. Bond lengths of the nitronyl nitroxide fragments are typical. In two independent diradical molecules, designated as **A** and **B**, a nitronyl nitroxide fragment and the nearest side thiophene ring lie almost in the same plane (see Table 1), which can be rationalized by the existence of short intramolecular hydrogen bonds O···H–C. As a result, this also leads to extremely short contacts (2.75–2.84 Å) between O atoms and S atoms of the fused sulfur-containing heteropentacene (Table 1). The heteropentacene backbone in molecule **A** is noticeably bent so the angle between mean planes of side thiophene rings exceeds 14°.

Each independent molecule has short intermolecular contacts with a member of the neighboring pair; this interaction leads to formation of centrosymmetrical dimers **A**···**A** and **B**···**B** (Figure 6a,b). The alternating dimers **A**···**A** and **B**···**B** form inclined stacks with a short interdimer contact S···S (3.58 Å, Figure 6c). Finally, the stacks are surrounded by interdigitating dodecyl chains (Figure S8 in the Supporting Information).

The crystal structure analysis showed that the characteristic feature of both the mono- and diradical is formation of edge-to-edge dimers (even two types of dimers in the case of diradical NN_2-DT*m*BDT) followed by their packing in stacks. This feature is absent in the case of the precursor, Br_2-DT*m*BDT, which forms dyads in a face-to-face manner upon crystallization.[16] Thus, the introduction of nitronyl nitroxide radical groups into

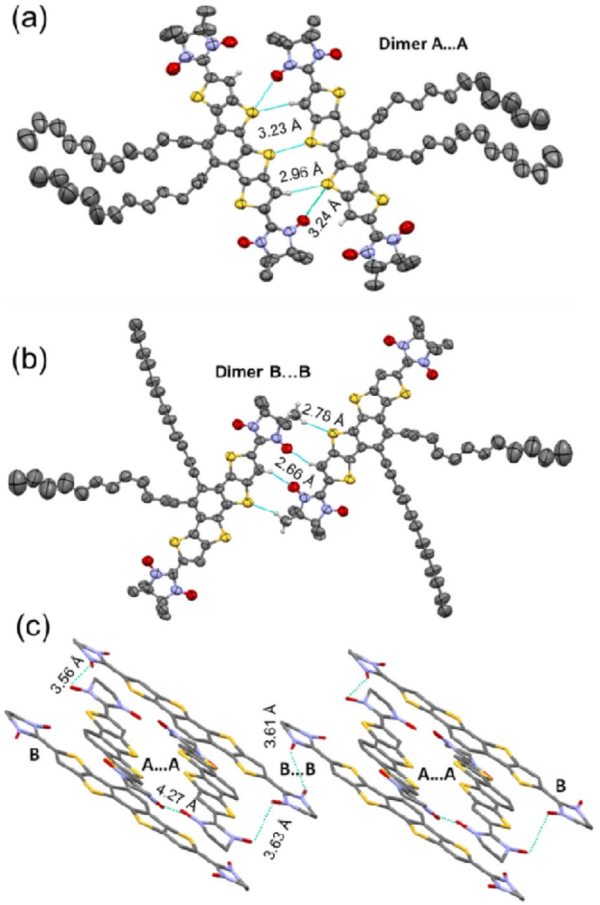

Figure 6. a and b) Dimers **A**···**A** and **B**···**B** in the crystals of diradical NN_2-DT*m*BDT with thermal ellipsoids drawn at the 50% probability level (most H atoms are omitted for clarity). c) Relative arrangement of the dimers **A**···**A** and **B**···**B** in stacks with O···O contacts < 4.27 Å (alkyl groups are omitted).

DT*m*BDT considerably changes the network of van der Waals forces in such a way that formation of the edge-to-edge dimers becomes preferable. A similar tendency was also observed in nitronyl nitroxide diradicals coupled with other fused-thiophenes, such as thieno[2,3-*b*]thiophene and thieno[3,2-*b*]thiophene.[9] Therefore, an appropriate combination of the nitronyl nitroxide and fused-thiophene moieties could be viewed as a useful crystal engineering tool for creation of structures of organic paramagnets and their magnetic substructures as well.

The magnetic motif of NNBr-DT*m*BDT arises from the short intermolecular contacts $O_{NO}\cdots H{-}C_{Me}$ (2.54 Å) leading to formation of spin chains. According to BS-UB3LYP calculations, the exchange interaction in this pair is weak and antiferromagnetic with $J=-0.13\ cm^{-1}$ (or −0.2 K).

The magnetic motif of crystalline NN_2-DT*m*BDT is rather complicated and includes the intramolecular exchange channels within **A** and **B** diradicals, then intradimer exchange channels **A**···**A** and **B**···**B** through two corresponding contacts of 4.27 Å and one contact of 3.61 Å between nitroxide oxygens and, in addition, interdimer exchange channels through contacts 3.56 and 3.63 Å between nitroxide oxygens (Figure 6c). To analyze each channel, the intra- and intermolecular exchange interactions were calculated for the XRD structures.

The intermolecular exchange interactions were calculated only at the BS-UB3LYP level because this approach works well for nitroxides.[29] According to the calculations, the spin density in the triplet state is localized almost exclusively at the nitronyl nitroxide moieties (Figure S15a in the Supporting Information). Taking this into account, we estimated the exchange interactions in a pair of diradicals by calculations for a pair of model radicals obtained by replacing the remote nitronyl nitroxide moiety by a diamagnetic analog (Figure S15 in the Supporting Information). According to the calculations, the intradimer interactions are ferromagnetic but very weak (Table 2). Weak ferromagnetic and moderate antiferromagnetic exchange interactions were obtained for diradicals of different types (**A**···**B**, Table 2).

In contrast to intermolecular exchange interactions, the BS-DFT approach often overestimates the exchange interaction parameters $|J|$ for diradicals,[30] and high-level calculations should be used in this case. Indeed, the BS-DFT calculations predict a moderate antiferromagnetic exchange for both isomers of the NN_2-DT*m*BDT diradical. On the other hand, much more expensive and accurate calculations predict negligible antiferromagnetic interactions (Table 3).

Table 2. Parameters of the exchange interaction (*J*) between neighboring diradicals, which was calculated at the BS-UB3LYP/def2-TZVP level of theory.

Contact	*R*(O···O) [Å]	*J* [cm^{-1}]
AA	4.274	0.2
AB1	3.557	2.1
AB2	3.634	−23.1
BB	3.611	0.5

Table 3. Parameters (*J*) of the intramolecular exchange interaction for the isomers **A** and **B** of diradical NN_2-DT*m*BDT calculated at different levels of theory.

Conformer	*J* [cm^{-1}] BS-UB3LYP/ def2-TZVP	CASSCF(10,10)[a]/ def2-SVP	NEVPT2(10,10)/ def2-SVP
A	−29.3	−1.0	−2.0
B	−53.0	−2.8	−4.0

[a] Active spaces for these calculations are presented in the Supporting Information (Tables S3 and S4).

Differential scanning calorimetry (DSC) analysis of polycrystalline samples revealed that before melting (155–158 °C) the NNBr-DT*m*BDT monoradical undergoes two reversible PTs accompanied by hysteresis: a PT at approximately 15 and 12 °C during heating and cooling, respectively; and a PT at approximately 85 and 80 °C (Figure 7a and Figure S9 in the Supporting Information). As to the diradical NN_2-DT*m*BDT melting at 230–232 °C, it showed a reversible PT also accompanied by hysteresis at approximately 11 °C (heating) and 2 °C (cooling), as well as an irreversible PT in the temperature range 130–

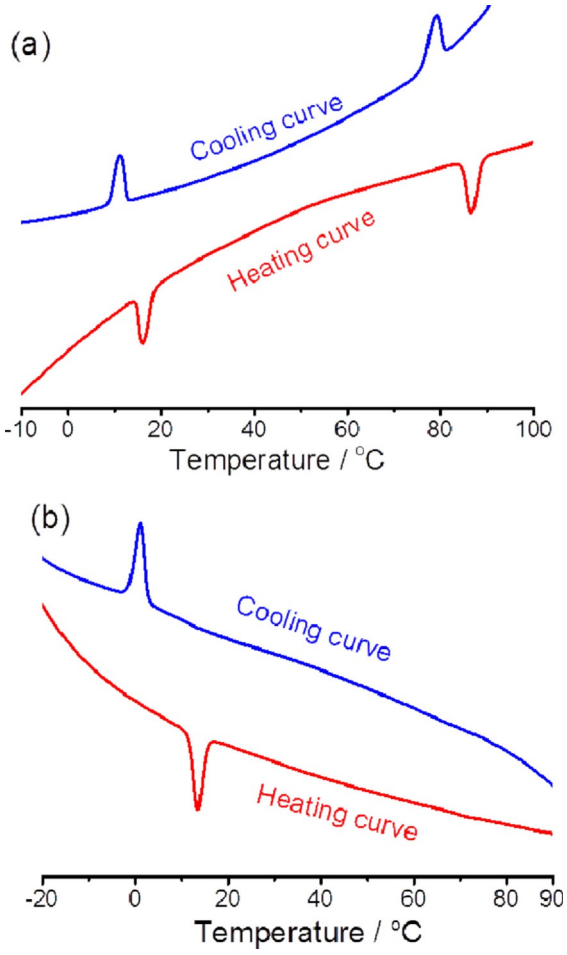

Figure 7. Fragments of DSC curves for the polycrystalline samples of monoradical NNBr-DT*m*BDT (a) and diradical NN_2-DT*m*BDT (b) measured in a nitrogen atmosphere at a heating rate of 10 °C min^{-1}.

140 °C (Figure 7b and Figure S10 in the Supporting Information). It is worth noting that similar PTs are absent in the Br_2-DT*m*BDT crystals; in the first DSC cycle, the dibromo-derivative showed prominent peaks only at 130 and 50 °C in response to melting and crystallization, respectively. The only feature, an opposite peak at 64 °C, appears during heating in the second and subsequent cycles and could be due to the crystallization giving rise to a new phase melting at 98 °C (Figure S11 in the Supporting Information).

Intrigued by this observation in the DSC analysis, we conducted XRD analysis of a single crystal of monoradical NNBr-DT*m*BDT at 30 °C to detect changes in the lattice parameters. We observed a significant increase in the unit cell volume from 2247 Å^3 (measured at −143 °C) to 2331 Å^3 (measured at 30 °C) with the following alteration in the unit cell parameters: lengths *a* (6.09 to 6.34 Å), *b* (13.17 to 13.35 Å), *c* (28.71 to 28.59 Å) and angles α (78.5 to 76.4°), β (89.8 to 85.5°), and γ (84.0 to 82.4°) on going from −143 °C to 30 °C. Moreover, the space group ($P\bar{1}$) remained the same at both temperatures. Attempts to solve the structure of the high-temperature phase for NNBr-DT*m*BDT (at 100 °C) and for diradical NN_2-DT*m*BDT (at 30 °C) were not successful because of the poor quality of the diffraction data.

Variable-temperature FTIR microscopy was found to be a suitable tool for probing the PTs in the NNBr-DT*m*BDT and NN_2-DT*m*BDT crystals. Figure 8a depicts the FTIR spectra of the NNBr-DT*m*BDT thin single crystal analyzed at temperatures below and above the PTs. Wavenumbers of the maxima of the most intense vibrational bands are depicted in the plot. One can see that PTs taking place in NNBr-DT*m*BDT do not significantly influence the positions of the bands; this result implies that the structural changes are less significant, for example, in comparison with magneto-active copper(II)-nitroxide complexes.[31] Nevertheless, the intensity and shape of some bands were strongly affected by these changes (C–H stretching modes and bands at approximately 1470, 840, and 718 cm^{-1}). Among them, the vibration band at approximately 1470 cm^{-1}, attributed to the C–C stretching vibration mode, clearly reflects the PT (Figure 8b). At a low temperature (80 K), this band is quite intense, and its intensity slightly decreases up to the temperature of the first PT (≈283 K). When the PT takes place, the intensity of the band drops in a stepwise manner and the band maximum is slightly shifted. A further increase in the temperature up to the second PT leads to a slight decrease in the band intensity (≈1470 cm^{-1}). When the second PT takes place, the intensity of the band drops again, and the band

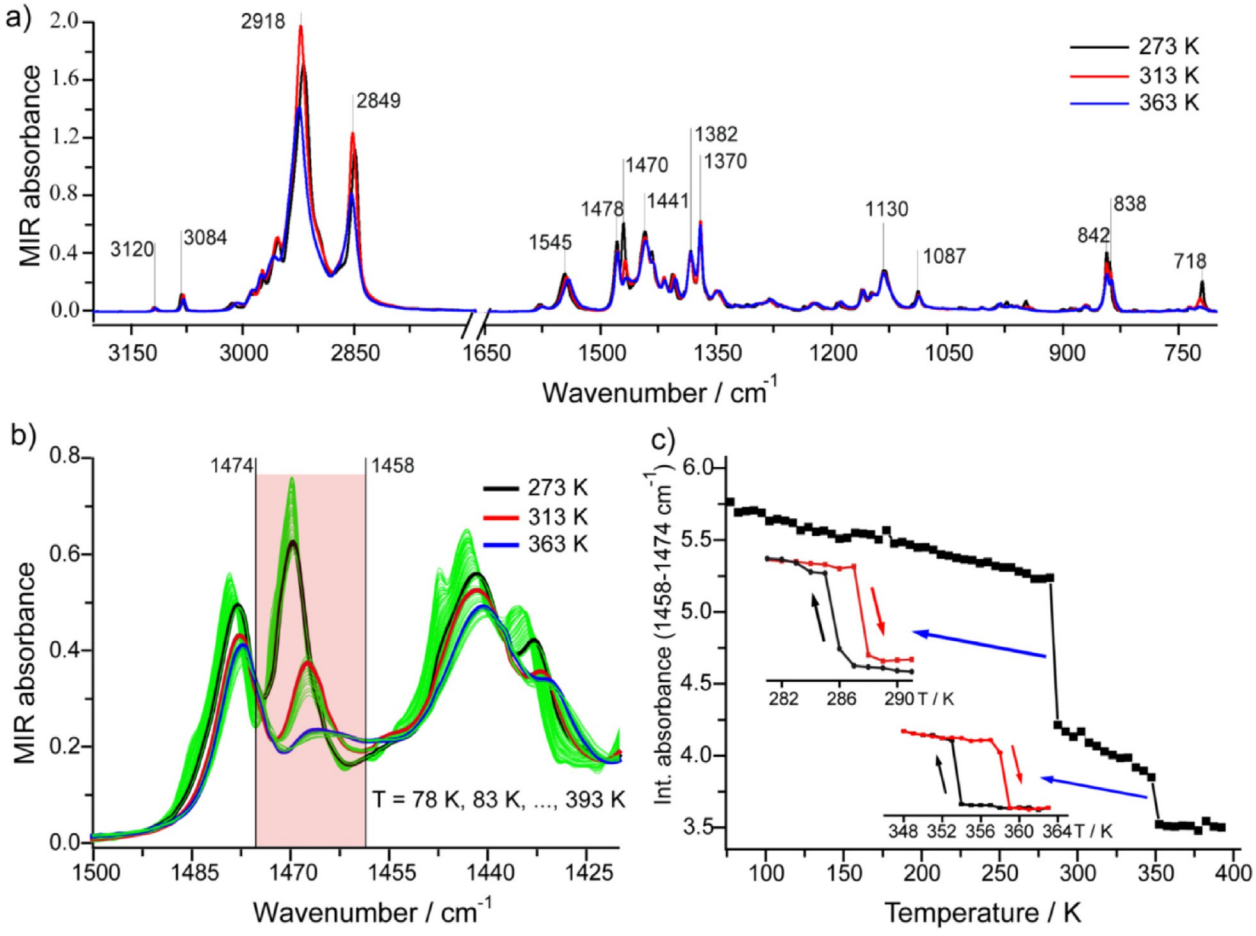

Figure 8. a) FTIR spectra of the NNBr-DT*m*BDT thin single crystal measured in a mid-IR range at temperatures 273, 313, and 363 K. b) Temperature dependence of the fragment of the FTIR spectra of NNBr-DT*m*BDT that were acquired within the temperature range 78–393 K (green), with three spectra highlighted. The area used for the spectra integration is pink. c) Temperature dependence of the integrals calculated within the 1474–1458 cm^{-1} range. The reversibility of both transitions is shown as insets.

transforms to a broad baseline-like absorption pattern. Further heating of the sample up to 393 K does not induce any strong changes in the spectra. To visualize the changes of the vibrational band described, the temperature dependence of its integral absorbance is shown in Figure 8c. The integration was performed in the range 1474–1458 cm^{-1} as depicted in Figure 8b. The reversibility of both transitions was checked as shown in the insets in Figure 8c.

FTIR spectra of a thin single crystal of NN_2-DT*m*BDT are presented in Figure 9a in the same way as for NNBr-DT*m*BDT: at temperatures below and above the PTs. In contrast to NNBr-DT*m*BDT, the high-temperature PT for the diradical is irreversible and strongly affects most of the vibrational bands of the

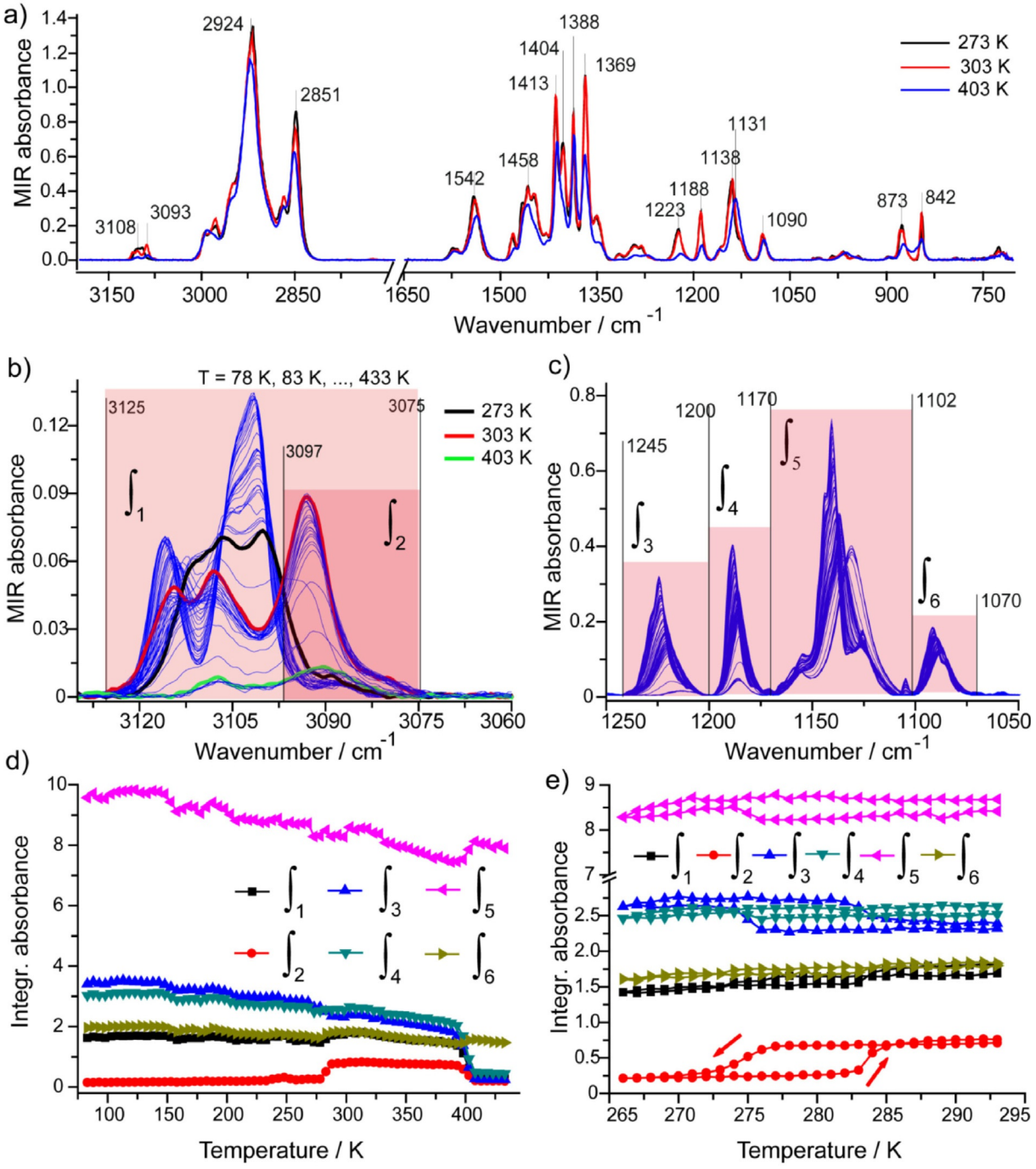

Figure 9. a) FTIR spectra of the NN_2-DT*m*BDT thin single crystal that were acquired in a mid-IR range at temperatures 273, 303, and 403 K. b) Temperature dependence of the high-energy fragment of the FTIR spectra of NN_2-DT*m*BDT analyzed within the temperature range 78–433 K (blue) with three spectra highlighted. The areas used for the spectra integration are pink. c) Temperature dependence of the fragment of the NN_2-DT*m*BDT FTIR spectra attributed to the C–C stretching vibrational band. The areas used for the spectra integration are highlighted in pink. d) Temperature dependence of integrals $\int_1,\ldots,\int_6$ obtained upon heating of the sample from 78 to 403 K. e) Temperature dependence of the integrals $\int_1,\ldots,\int_6$ obtained near the temperature of the first PT after heating and cooling of the sample.

FTIR spectra. To trace these changes, several vibrational bands (Figure 9b,c) were integrated in the following ranges: $\int_1$(3125–3075 cm^{-1}), $\int_2$(3097–3075 cm^{-1}), $\int_3$(1245–1200 cm^{-1}), $\int_4$(1200–1170 cm^{-1}), $\int_5$(1170–1102 cm^{-1}), and $\int_6$(1102–1070 cm^{-1}). The temperature dependences of these integrals after heating the sample from 78 to 433 K are shown in Figure 9d. The reversibility of the first PT at approximately 280 K is shown in Figure 9e.

The PTs observed in NNBr-DT*m*BDT and NN_2-DT*m*BDT may affect the intramolecular exchange interactions in diradicals and intermolecular exchange in dimers of radicals and diradicals and even the amount of paramagnetic species (e.g. in the case of a high-temperature irreversible PT). To gain further insights, variable-temperature (VT) continuous-wave (CW) EPR spectra of polycrystalline powder samples were measured at X-band (9.27 GHz) in a temperature range of 205–390 K (NNBr-DT*m*BDT) or 215–430 K (NN_2-DT*m*BDT); in the latter case, the subsequent cooling to 215 K was also recorded.

Figure 10 shows the EPR spectra of NNBr-DT*m*BDT (polycrystalline powder) recorded in the temperature range 205–390 K. One can see that the shape of the observed curve is not affected by the PTs. The monotonic decrease in the double integral of the EPR spectra (Figure S13 in the Supporting Information) after heating the sample is mainly caused by changes in the Boltzmann population of the spin levels (but also can be partially caused by some instrumental factors, e.g. a Q-value change in the MW resonator). The shift of the spectra is small relative to its linewidth, and in the whole temperature range $g = 2.006 \pm 0.001$. The linewidth of the NNBr-DT*m*BDT signal (Figure 12) slightly increases from 1.05 mT (205 K) to 1.15 mT (390 K), which is typical of organic radicals because of the shortening of the spin relaxation time after heating of the sample. Thus, PTs proceeding in NNBr-DT*m*BDT do not influence the magnetic resonance parameters of the embedded nitroxide radicals.

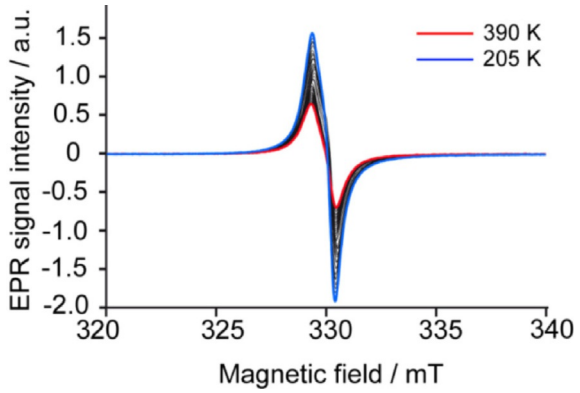

Figure 10. Temperature dependence of the EPR spectra of NNBr-DT*m*BDT analyzed at 9.27 GHz in the temperature range 205–390 K with 5 K steps.

In contrast to NNBr-DT*m*BDT, the EPR spectra of NN_2-DT*m*BDT (polycrystalline powder) are sensitive to both PTs after heating. Although only one strong change in the spectra shape is clearly visible in Figure 11a, the temperature dependence of the linewidth unambiguously indicates two stepwise changes. Most likely, owing to the efficient intra- and intermolecular exchange interactions, the linewidth of NN_2-DT*m*BDT is always smaller than that of NNBr-DT*m*BDT (exchange narrowing) and decreases to almost 0.4 mT at approximately 320 K (Figure 12).

The linewidth increases to 0.7 mT when the first PT takes place. The second PT leads to a further increase in linewidth to 0.85 mT. Cooling down the NN_2-DT*m*BDT sample from 430 to 215 K did not induce any meaningful changes in the spectra shape (Figure 11b) and showed only a slight monotonic increase in the linewidth to 0.92 mT (Figure 12). The temperature dependence of the double integral of NN_2-DT*m*BDT EPR spectra does not reveal correlations with the PTs, but shows behavior similar to that of NNBr-DT*m*BDT (Figure S14 in the Supporting Information). Remarkably, the irreversible PT does not reduce the number of unpaired electrons in the NN_2-DT*m*BDT, although both PTs influence intra- or/and intermolecular exchange spin–spin interactions, resulting in a change of the linewidth of the EPR spectrum.

3. Conclusions

We successfully synthesized the first neutral paramagnetic dithieno[2,3-*d*;2′,3′-*d*′]benzo-[1,2-*b*;3,4-*b*′]dithiophene derivatives functionalized with mono- (NNBr-DT*m*BDT) and dinitronyl ni-

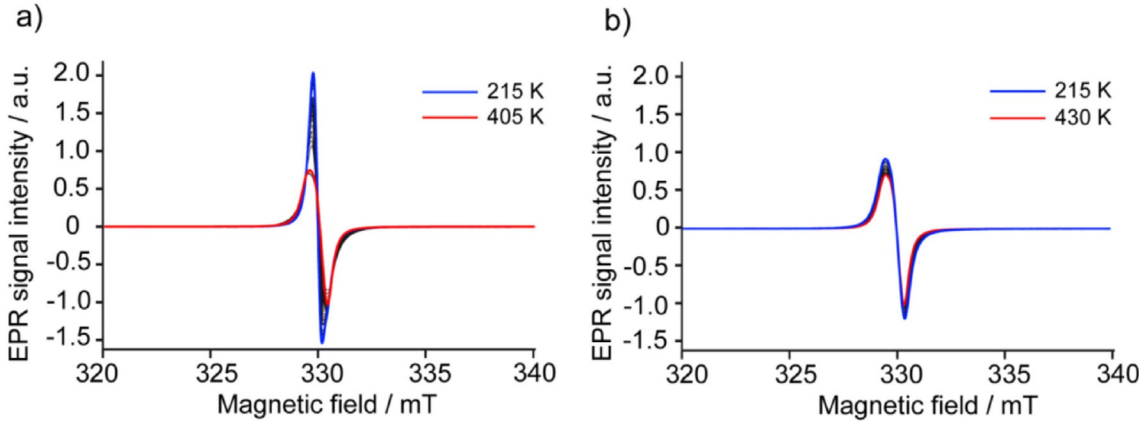

Figure 11. a) Temperature dependence of the EPR spectra of NN_2-DT*m*BDT that were acquired at 9.27 GHz in the temperature range 215–430 K (heating) and with b) subsequent cooling of the NN_2-DT*m*BDT sample to 215 K. In both cases, the spectra were acquired with a temperature step of 5 K.

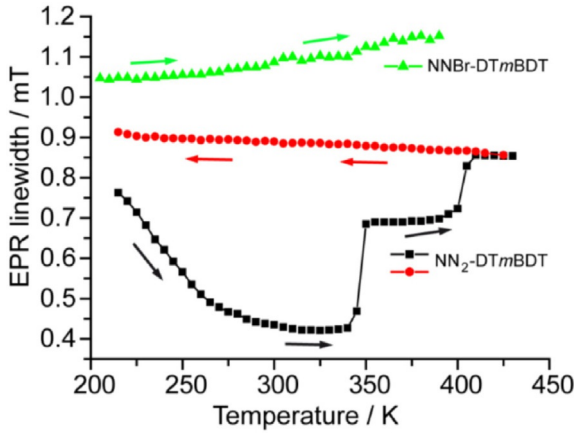

Figure 12. Temperature dependence of the EPR linewidth of NNBr-DT*m*BDT and NN_2-DT*m*BDT. Arrows show the direction of the temperature changes.

troxide (NN_2-DT*m*BDT) radical moieties. The adequate stability of both nitroxides allowed us to study their structural, optoelectronic, electrochemical, and magnetic properties. NNBr-DT*m*BDT and NN_2-DT*m*BDT were found to form edge-to-edge dimers, which then organized into close π-stacks surrounded by interdigitating dodecyl chains. At lower temperatures, the mono- and diradicals undergo reversible solid-state PTs accompanied by hysteresis. At higher temperatures, both paramagnets show an additional solid-state PT: in the mononitroxide it is reversible and accompanied by a hysteresis, whereas in the diradical, it takes place at higher temperatures than the monoradical and it is irreversible. It is noteworthy that the crystal structure of the dibromo-precursor is formed by face-to-face dyads, and no solid-state PTs were detected. Hence, the attachment of nitronyl nitroxide groups to the DT*m*BDT skeleton significantly changes its packing morphology and temperature-dependent structural dynamics.

Experimental Section

General Methods

All the reagents were purchased from commercial sources and used without further purification unless stated otherwise. Column chromatography was performed by using Merck silica gel 60, 40–63 μm (230–400 mesh). Thin-layer chromatography was carried out by using precoated aluminum sheets with silica gel 60 F254 (Merck).

Sample Characterization

Infrared spectroscopy was conducted with a Nicolet 730 FTIR spectrometer equipped with an attenuated total reflection (ATR) setup. The samples were deposited as pristine material on the diamond crystal and pressed onto it with a stamp. Measurements with a scan number of 128 were run for each sample, and the background was subtracted. The UV/Vis spectra were recorded at 298 K with a Perking-Elmer Lambda 900 spectrophotometer. Matrix-assisted laser desorption ionization time-of-flight (MALDI-TOF) mass spectra were acquired with a Bruker Reflex II MALDI-TOF mass spectrometer, calibrated against a mixture of C_{60}/C_{70}. Differential scanning calorimetry (DSC) was carried out with a Mettler DSC 30 analyzer with heating rates of 10 K min^{-1}. Cyclic voltammetry (CV) measurements were carried out with a computer-controlled GSTAT12 within a three-electrode cell in a CH_2Cl_2 solution of Bu_4NPF_6 (0.1 M) at a scan rate of 100 mV s^{-1} at room temperature, by means of a Pt disc as the working electrode, Pt wire as the counter electrode, and an Ag electrode as the reference electrode. The potentials were determined by using ferrocene (Fc) as a standard. The X-ray crystallographic data for the molecules were collected with a Smart CCD diffractometer using a $Mo_{K\alpha}$ graphite monochromator radiation source. CCDC 1497768 (for monoradical NNBr-DT*m*BDT) and 1497769 (for diradical NN_2-DT*m*BDT) contain the supplementary crystallographic data for this paper. These data are provided free of charge by The Cambridge Crystallographic Data Centre.

Synthesis

Di(5-bromothieno)[2,3-*d*;2′,3′-*d*′]-4,5-didodecylbenzo[2,1-*b*:3,4-*b*′]dithiophene (Br_2-DT*m*BDT),[16] 4,4,5,5-tetramethyl-4,5-dihydro-1*H*-imidazol-3-oxid-1-oxyl,[32,33] and triphenylphosphine-gold(I)-(4,4,5,5-tetramethyl-4,5-dihydro-3-oxid-1-oxyl-1*H*-imidazol-2-ide) were synthesized according to previous reports.

(5-Bromothieno)[2,3-d]-(5-(4,4,5,5-tetramethyl-4,5-dihydro-3-oxid-1-oxyl-1H-imidazol-2-yl)thieno)[2′,3′-d′]-4,5-didodecylbenzo[2,1-b:3,4-b′]dithiophene (NNBr-DTmBDT)

A solution of dibromide Br_2-DT*m*BDT (32 mg, 0.040 mmol), nitronyl nitroxide gold complex (27 mg, 0.043 mmol), and $[Pd(PPh_3)_4]$ (8 mg) in THF (5 mL) was stirred at 60–65 °C in an argon atmosphere for 2 h. The solvent was evaporated, and the residue was purified by column chromatography on silica gel by using ethyl acetate as an eluent. Two green fractions were collected and evaporated. The residues were dissolved in hot hexane, and the solutions were filtered and evaporated. Crude products were recrystallized two or three times from a mixture of CH_2Cl_2 with MeOH to obtain monoradical NNBr-DT*m*BDT (15 mg, 43%) and diradical NN_2-DT*m*BDT (5 mg, 13%). Monoradical NNBr-DT*m*BDT: thin green plates; m.p.: 155–158 °C; R_f = 0.71 (ethyl acetate); IR: υ = 2920, 2850, 1545, 1464, 1442, 1417, 1403, 1383, 1367, 1350, 1220, 1188, 1157, 1132, 1090, 870, 841, 808, 719, 617, 598, 540, 514 cm^{-1}; UV/Vis (toluene): λ_{max} ($\varepsilon \times 10^{-2}$) = 357 sh (180), 374 (280), 395 (260), 635 (1.7), 700 (2.5), 779 nm^{-1} (1.5); MALDI-TOF MS: *m/z* calcd. (%) for $C_{45}H_{64}BrN_2O_2S_4$: 871.3 (100) $[M]^+$, 873.3 (97) $[M+2]^+$; found: 873 (average M_W); elemental analysis calcd.: C 61.90, H 7.39, N 3.21; found: C 61.86, H 7.50, N 3.07.

Di-(5-(4,4,5,5-tetramethyl-4,5-dihydro-3-oxid-1-oxyl-1H-imidazol-2-yl)thieno)[2,3-d;2′,3′-d′]-4,5-didodecylbenzo[2,1-b:3,4-b′]dithiophene (NN_2-DTmBDT)

A solution of dibromide Br_2-DT*m*BDT (30 mg, 0.038 mmol), nitronyl nitroxide gold complex (80 mg, 0.13 mmol), and $[Pd(PPh_3)_4]$ (8 mg) in THF (10 mL) was stirred at 60–65 °C in an argon atmosphere for 16 h. The same purification procedure as above yielded monoradical NNBr-DT*m*BDT (4 mg, 12%) and diradical NN_2-DT*m*BDT (22 mg, 61%). Diradical NN_2-DT*m*BDT: voluminous crystals of intense green color; decomp. at 210 °C; R_f = 0.26 (ethyl acetate); IR: υ = 2923, 2852, 1544, 1448, 1408, 1386, 1367, 1221, 1186, 1160, 1135, 1089, 1004, 962, 872, 844, 719, 617, 600, 540, 512 cm^{-1}; UV/Vis (toluene): λ_{max} ($\varepsilon \times 10^{-2}$): 377 sh (190), 395 (330), 420 (350), 635 (3.5), 700 (4.4),

779 nm^{-1} (2.8); MALDI-TOF MS: *m/z* calcd. (%) for $C_{52}H_{76}N_4O_4S_4$: 948.5 (100) $[M]^+$, 949.5 (60) $[M+1]^+$; found: 949 (average M_w); elemental analysis calcd.: C 65.78, H 8.07, N 5.90; found: C 65.86, H 8.05, N 6.07.

Analysis of PTs

DSC was conducted with a Mettler DSC 30 at heating and cooling rates of 10 $K\,min^{-1}$. EPR measurements were carried out in CW mode by using a commercial Bruker EMX X-band EPR spectrometer (Bruker BioSpin, Germany) equipped with a gas flow ER 4131VT temperature control system ($T = 90$–450 K), where boiling liquid nitrogen served as a gas source. The microwave frequency and microwave power used in the experiments were 9.27 GHz and 0.2 mW, respectively. The magnetic field modulation frequency and amplitude were 100 kHz and 0.2 mT, respectively. The temperature dependence of the EPR spectra of the polycrystalline powder samples mixed with a KBr powder (to increase the homogeneity) were recorded with a step of 5 K. Double integrals and the linewidth of the spectra were calculated. The linewidth was determined as the difference in the fields of extrema of the experimental EPR spectrum.

FTIR spectra of thin single crystals were acquired in the mid-IR in the temperature range 80–475 K. The temperature dependences of the IR spectra were obtained with a step of 5 K, whereas the reversibility of the PTs was verified at a temperature step of 1 K. Near the PT temperatures, spectra were recorded in the range 4000–700 cm^{-1} by using an infrared microscope HYPERION 2000 (Bruker Optics, Germany) equipped with MCT detector D316 and coupled to a FTIR spectrometer Bruker Vertex 80v. The spectral resolution was 1 cm^{-1}. A sample stage Linkam FTIR600 (Linkam Scientific Instruments, United Kingdom) equipped with BaF_2 windows was used to control the temperature of the single crystals.

DFT and Ab Initio Calculations

All the calculations were performed by using geometries of the radicals NNBr-DT*m*BDT and diradicals NN_2-DT*m*BDT, their dimers, and pairs from the XRD data; dodecyl tails were replaced by methyl groups to save the computational resources. The ORCA package was used for all the calculations.[34]

The spin–spin part of the zero-field splitting (ZFS) parameters (*D* and *E*) was computed at the ROBP86/def2-TZVP level of theory[35] by using the approach[36] implemented in the ORCA package.

Parameters of intra- and intermolecular exchange interactions $J\left(\hat{H} = -2J\vec{S}_1\vec{S}_2\right)$ were calculated by using the spin-unrestricted broken-symmetry approach[37] at the UB3LYP/def2-TZVP level of theory[38] by using the formula [Eq. (2)]:

$$J = -\left(E^{HS} - E^{LS}_{BS}\right) / \left(\langle S^2\rangle^{HS} - \langle S^2\rangle^{LS}_{BS}\right) \quad (2)$$

where indices HS and LS correspond to high-spin and broken-symmetry low-spin solutions, respectively. To clarify the intramolecular exchange interactions, singlet–triplet splitting in the diradicals was computed by the CASSCF and CASSCF/NEVPT2 procedures[39] with the def2-SVP basis.

The electronic absorption spectrum of the NNBr-DT*m*BDT radical was calculated by using a time-dependent DFT approach[40] with the B3LYP functional and def2-TZVP basis set.[41]

Acknowledgments

E.T. thanks the German Academic Exchange Service DAAD (programme Bilateral Exchange of Academics 2015/50015739) and FASO Russia (project 0302-2016-0002). M.F. thanks FASO Russia (project 0333-2016-0001). S.V. thanks the RF President's Grant MK-3597.2017.3. N.G. and D.G. acknowledge the Russian Foundation for Basic Research (project 15-03-03242) for support of the computational part. The authors are also grateful to Dr. Dieter Schollmeyer at Johannes Gutenberg-University, Mainz, for crystal structure analysis. A.K. and M.B. thank King Abdullazis City of Science and Technology (KACST) for financial support. A.K. is thankful to Prof. Klaus Müllen for his constant encouragement and support.

Conflict of Interest

The authors declare no conflict of interest.

Keywords: density functional and ab initio calculations · EPR spectroscopy · fused thiophene · nitronyl nitroxides · π-stacking

[1] J. S. Miller, *Angew. Chem. Int. Ed.* **2003**, *42*, 27 – 29; *Angew. Chem.* **2003**, *115*, 27 – 29.
[2] M. E. Itkis, X. Chi, A. W. Cordes, R. C. Haddon, *Science* **2002**, *296*, 1443 – 1445.
[3] X. Chi, M. E. Itkis, R. W. Reed, R. T. Oakley, A. W. Cordes, R. C. Haddon, *J. Phys. Chem. B* **2002**, *106*, 8278 – 8287.
[4] X. Chi, M. E. Itkis, K. Kirschbaum, A. A. Pinkerton, R. T. Oakley, A. W. Cordes, R. C. Haddon, *J. Am. Chem. Soc.* **2001**, *123*, 4041 – 4048.
[5] P. Ravat, T. Marszalek, W. Pisula, K. Müllen, M. Baumgarten, *J. Am. Chem. Soc.* **2014**, *136*, 12860 – 12863.
[6] Y. Kawanaka, A. Shimizu, T. Shinada, R. Tanaka, Y. Teki, *Angew. Chem. Int. Ed.* **2013**, *52*, 6643 – 6647; *Angew. Chem.* **2013**, *125*, 6775 – 6779.
[7] A. Ito, A. Shimizu, N. Kishida, Y. Kawanaka, D. Kosumi, H. Hashimoto, Y. Teki, *Angew. Chem. Int. Ed.* **2014**, *53*, 6715 – 6719; *Angew. Chem.* **2014**, *126*, 6833 – 6837.
[8] E. T. Chernick, R. N. Casillas, J. Zirzlmeier, D. M. Gardner, M. Gruber, H. Kropp, K. Meyer, M. R. Wasielewski, D. M. Guldi, R. R. Tykwinski, *J. Am. Chem. Soc.* **2015**, *137*, 857 – 863.
[9] E. Tretyakov, K. Okada, S. Suzuki, M. Baumgarten, G. Romanenko, A. Bogomyakov, V. Ovcharenko, *J. Phys. Org. Chem.* **2016**, *29*, 725 – 734.
[10] L. Biniek, B. C. Schroeder, J. E. Donaghey, N. Yaacobi Gross, R. S. Ashraf, Y. W. Soon, C. B. Nielsen, J. R. Durrant, T. D. Anthopoulos, I. McCulloch, *Macromolecules* **2013**, *46*, 727 – 735.
[11] C. Wetzel, E. Brier, A. Vogt, A. Mishra, E. Mena-Osteritz, P. Bäuerle, *Angew. Chem. Int. Ed.* **2015**, *54*, 12334 – 12338; *Angew. Chem.* **2015**, *127*, 12511 – 12515.
[12] Y. Tsutsui, T. Sakurai, S. Minami, K. Hirano, T. Satoh, W. Matsuda, K. Kato, M. Takata, M. Miura, S. Seki, *Phys. Chem. Chem. Phys.* **2015**, *17*, 9624 – 9628.
[13] J. Shaw, H. Zhong, C. P. Yau, A. Casey, E. Buchaca-Domingo, N. Stingelin, D. Sparrowe, W. Mitchell, M. Heeney, *Macromolecules* **2014**, *47*, 8602 – 8610.
[14] J. Zhang, K. Zhang, W. Zhang, Z. Mao, M. S. Wong, G. Yu, *J. Mater. Chem. B* **2015**, *3*, 10892 – 10897.
[15] L. Huo, T. Liu, X. Sun, Y. Cai, A. J. Heeger, Y. Sun, *Adv. Mater.* **2015**, *27*, 2938 – 2944.
[16] A. Keerthi, C. An, M. Li, T. Marszalek, A. G. Ricciardulli, B. Radha, F. D. Alsewailem, K. Müllen, M. Baumgarten, *Polym. Chem.* **2016**, *7*, 1545 – 1548.
[17] P. Gao, D. Beckmann, H. N. Tsao, X. Feng, V. Enkelmann, W. Pisula, K. Müllen, *Chem. Commun.* **2008**, 1548 – 1550.

[18] P. Gao, D. Beckmann, H. N. Tsao, X. Feng, V. Enkelmann, M. Baumgarten, W. Pisula, K. Müllen, *Adv. Mater.* **2009**, *21*, 213 – 216.
[19] L. Chen, M. Baumgarten, X. Guo, M. Li, T. Marszalek, F. D. Alsewailem, W. Pisula, K. Müllen, *J. Mater. Chem. B* **2014**, *2*, 3625 – 3630.
[20] R. Tanimoto, S. Suzuki, M. Kozaki, K. Okada, *Chem. Lett.* **2014**, *43*, 678 – 680.
[21] a) R. Beaulac, G. Bussiere, C. Reber, C. Lescopz, D. Luneau, *New J. Chem.* **2003**, *27*, 1200 – 1206; b) I. Yu. Barskaya, S. L. Veber, E. A. Suturina, P. S. Sherin, K. Yu. Maryunina, N. A. Artiukhova, E. V. Tretyakov, R. Z. Sagdeev, V. I. Ovcharenko, N. P. Gritsan, M. V. Fedin, *Dalton Trans.* **2017**, submitted.
[22] The departure of the value ΔE_p from the constant value of 59 mV expected for an electrochemically reversible one-electron transfer is due to experimental factors, as the value ΔE_p of the one-electron oxidation of Fc (reversible process) under the same experimental conditions is very similar (80 mV, see the Supporting Information), see: E. R. Brown, J. R. Sandifer, in *Physical Methods of Chemistry. Electrochemical Methods. Vol. 2* (Eds.: B. W. Rossiter, J. F. Hamilton), Wiley, New York, **1986**.
[23] T. R. Jow, K. Y. Jen, R. L. Elsenbaumer, L. W. Shacklette, M. Angelopoulos, M. P. Cava, *Synth. Met.* **1986**, *14*, 53 – 60.
[24] Oxidation potentials vs. Fc/Fc^+ for aryl-substituted dithieno[2,3-*d*;2′,3′-*d*′]-4,5-didodecylbenzo[2,1-*b*:3,4-*b*′]dithiophene ($\approx$0.66 V) is higher than ones typical for aryl-substituted nitronyl nitroxides, for example, +0.37 V for the phenyl-substituted nitronyl nitroxide (see S. Suzuki, H. Yokoi, M. Kozaki, Y. Kanzaki, D. Shiomi, K. Sato, T. Takui, K. Okada, *Eur. J. Inorg. Chem.* **2014**, 4740 – 4744).
[25] Y. B. Borozdina, Ph.D. Thesis, Johannes Gutenberg-Universität Mainz, Germany, **2012**.
[26] R. Ziessel, G. Ulrich, R. C. Lawson, L. Echegoyen, *J. Mater. Chem.* **1999**, *9*, 1435 – 1448.
[27] S. S. Eaton, K. M. More, B. M. Sawant, G. R. Eaton, *J. Am. Chem. Soc.* **1983**, *105*, 6560 – 6567.
[28] E. V. Tretyakov, V. I. Ovcharenko, *Russ. Chem. Rev.* **2009**, *78*, 971 – 1012.
[29] a) M. V. Fedin, S. L. Veber, K. Y. Maryunina, E. A. Suturina, N. P. Gritsan, R. Z. Sagdeev, V. I. Ovcharenko, E. G. Bagryanskaya, *J. Am. Chem. Soc.* **2010**, *132*, 13886 – 13891; b) S. E. Tolstikov, E. V. Tretyakov, D. G. Mazhukin, I. F. Zhurko, M. V. Fedin, G. V. Romanenko, A. S. Bogomyakov, D. E. Gorbunov, N. P. Gritsan, *Chem. Eur. J.* **2016**, *22*, 14598 – 14604.
[30] S. Tolstikov, E. Tretyakov, S. Fokin, E. Suturina, G. Romanen-ko, A. Bogomyakov, D. Stass, A. Maryasov, N. Gritsan, V. Ovcharenko, *Chem. Eur. J.* **2014**, *20*, 2793 – 2803.
[31] S. L. Veber, E. A. Suturina, M. V. Fedin, K. N. Boldyrev, K. Y. Maryunina, R. Z. Sagdeev, V. I. Ovcharenko, N. P. Gritsan, E. G. Bagryanskaya, *Inorg. Chem.* **2015**, *54*, 3446 – 3455.
[32] D. G. B. Boocock, R. Darcy, E. F. Ullman, *J. Am. Chem. Soc.* **1968**, *90*, 5945 – 5946.
[33] E. V. Tretyakov, I. A. Utepova, M. V. Varaksin, S. E. Tolstikov, G. V. Romanenko, A. S. Bogomyakov, D. V. Stass, V. I. Ovcharenko, O. N. Chupakhin, *ARKIVOC (Gainesville, FL, U.S.)* **2011**, 76 – 98.
[34] a) F. Neese, *WIREs Comput. Mol. Sci.* **2012**, *2*, 73 – 78; b) F. Neese, *ORCA—An Ab Initio, Density Functional and Semiempirical Program Package*, *Version 3.0.3*, Max Planck Institute for Bioinorganic Chemistry, Mulheim, Germany, **2016**.
[35] a) A. D. Becke, *Phys. Rev. A* **1988**, *38*, 3098 – 3100; b) J. P. Perdew, *Phys. Rev. B* **1986**, *33*, 8822 – 8824.
[36] a) F. Neese, *J. Am. Chem. Soc.* **2006**, *128*, 10213 – 10222; b) D. Ganyushin, F. Neese, *J. Chem. Phys.* **2006**, *125*, 024103.
[37] T. Soda, Y. Kitagawa, T. Onishi, Y. Takano, Y. Shigeta, H. Nagao, Y. Yoshioka, K. Yamaguchi, *Chem. Phys. Lett.* **2000**, *319*, 223 – 230.
[38] a) A. D. Becke, *J. Chem. Phys.* **1993**, *98*, 5648 – 5652; b) C. Lee, W. Yang, R. G. Parr, *Phys. Rev. B* **1988**, *37*, 785 – 789.
[39] a) C. Angeli, R. Cimiraglia, S. Evangelisti, T. Leininger, J.-P. Malrieu, *J. Chem. Phys.* **2001**, *114*, 10252 – 10264; b) C. Angeli, R. Cimiraglia, J.-P. Malrieu, *J. Chem. Phys.* **2002**, *117*, 9138 – 9153.
[40] A. Dreuw, M. Head-Gordon, *Chem. Rev.* **2005**, *105*, 4009 – 4037.
[41] F. Weigend, R. Ahlrichs, *Phys. Chem. Chem. Phys.* **2005**, *7*, 3297 – 3305.

Received: June 2, 2017
Revised manuscript received: July 20, 2017
Version of record online August 30, 2017

